RSC Advances

PAPER

View Article Online
View Journal | View Issue

Cite this: *RSC Adv.*, 2024, **14**, 28957

Mechanism of two styryl BODIPYs as fluorescent probes and protective agents in lipid bilayers against aqueous ClO^-†

Lu Yang,‡ Yanglin Jiang,‡ Ailin Sun, Mingqing Chen, Qiwei Li, Peng Wang * and Jianping Zhang

Received 9th May 2024
Accepted 18th August 2024

DOI: 10.1039/d4ra03433c

rsc.li/rsc-advances

Two styryl BODIPY derivatives, BOH and BOE, with different hydrophilic properties, were investigated for their reaction mechanisms in lipid bilayers against aqueous ClO^-, by both experimental and theoretical methods. Density functional theory (DFT) calculations confirmed their identical conformations in solution. Fluorescence spectra and high-resolution mass spectra corroborated the central vinyl group as a common antioxidation moiety against ClO^- oxidation. In giant unilamellar vesicles (GUVs), distinct reaction kinetics with ClO^- suggested that BOE provided superior protective effects compared to BOH on lipids. Molecular dynamics simulations indicated that the lipophilic octyloxy group in BOE led to its deeper localization within the lipid phase, bringing it closer to the corresponding lipid target group. This study establishes the two styryl BODIPYs as promising fluorescent probes for detecting aqueous ClO^- in lipid-water polyphasic systems.

1 Introduction

Hypochlorous acid (HOCl), recognized as a highly efficient and universal disinfectant in clinical practice,[1] also plays a vital role in the immune systems of animals and humans.[2,3] Endogenously generated HOCl serves as a significant reactive oxygen species (ROS), with concentrations *in vivo* ranging from 20 to 400 μM per hour,[4] which reacts with various biologically important molecules[5,6] and contributes to the pathogenesis of numerous diseases.[7–9] The development of rapid and effective methods for detecting HOCl, particularly *in situ in vivo*, holds significant implications for understanding its biological functions.[10–14] Among the various approaches to detect HOCl, fluorescence molecular probes stand out prominently.

Boradiazaindacene (BODIPY) derivatives, characterized by their highly fluorescent quantum yield, robust photo-stability, biocompatibility, and facile chemical modification, have emerged as one of the most appealing structural platforms. Specifically, styryl BODIPYs, featuring extended π-conjugation systems and chemically sensitive groups, have garnered considerable attention for their probing capabilities. For instance, oxidation of the central vinyl group in styryl phenol BODIPY derivatives enables their use as colorimetric and ratiometric fluorescent probes for selectively detecting Fe^{3+}[15,16] and Au^{3+}.[17] Another derivative serves as an 'on-off' fluorescent probe for Hg^{2+} by modulating the intramolecular charge transfer process.[18] Thiolysis of protective groups activates fluorescence emission, allowing styryl BODIPY derivatives to selectively probe H_2S[19] and cysteine[20] in living cells and tissues. Furthermore, reduction of nitro groups to amine groups under hypoxic conditions triggers a 'turn-on' fluorescence response, enabling imaging of hypoxic cells.[21] Other applications include two-photon fluorescent probes for dynamic imaging of redox balance[22] and near-infrared photoacoustic probes for reversible imaging of the ClO^-/GSH redox cycle *in vivo*.[23] Different strategies were reported to develop fluorescent probes based on BODIPY structures for selective detection of various ROS and RNS (reactive nitrogen species), *e.g.* H_2O_2,[24,25] NO,[26,27] HNO,[28] hydroxyl radical,[29] and HOCl,[30–37] *in vitro* and *in vivo*. Among them, a bi-styryl-BODIPY derivative was proved to be a fluorescent probe for HOCl imaging in living cells.[31]

Giant unilamellar vesicles (GUVs), *i.e.* liposomes with a diameter of 10–100 μm, can readily be viewed with conventional optical microscopy in an *in situ* and real-time manner.[38,39] Therefore, they have been widely employed as the model to study the physicochemical properties[40,41] and photooxidation[42,43] of biomembranes.

In this study, two styryl BODIPYs with differing hydrophilic substituents at the *ortho*-position of the C8-phenyl group, denoted as BOH and BOE, respectively, were synthesized. In comparison to in homogeneous ethanol–water solutions, the mechanisms of these two molecules embedded in giant unilamellar vesicles (GUVs) reacting with aqueous ClO^- were

Key Laboratory of Advanced Light Conversion Materials and Biophotonics, Department of Chemistry, School of Chemistry and Life Resources, Renmin University of China, Beijing 100872, China. E-mail: wpeng_chem@ruc.edu.cn; Tel: +86 10 62516604

† Electronic supplementary information (ESI) available. See DOI: https://doi.org/10.1039/d4ra03433c

‡ These authors contributed equally to this work.

investigated using experimental and theoretical approaches. The findings address key questions regarding the differential behaviours of these two molecules embedded in lipid bilayers when reacting with aqueous ClO^- and elucidate the underlying mechanisms governing their performance differences. This work provides valuable insights for designing related fluorescent probes.

2 Materials and methods

2.1 Materials and instruments

2,4-Dimethylpyrrole (97%), 4-*n*-octyloxybenzaldehyde, 2,3-dichloro-5,6-dicyano-1,4-benzoquinone (DDQ, 98%), *p*-hydroxybenzaldehyde (98%), n-octanol (99.5%), glacial acetic acid (99.5%); and triethylamine (Et_3N), boron trifluoride ether (BF_3OEt_2), sodium hypochlorite solution, piperidine, trifluoroacetic acid (TFA), and tetrahydrofuran (THF) all in analytical reagents (99%) were purchased from Aladdin Industries (Shanghai, China). L-alpha-phosphatidylcholine (PC, 14–29%, a mixture of various phospholipids) was purchased from Sigma Aldrich (St. Louis, Missouri, USA); Agarose with gelling range of 37 ± 1.5 °C was purchased from Baygene (Shanghai, China); Sucrose (≥99.5%) was purchased from Innochem (Beijing, China). All other reagents and solvents were obtained from Beijing Tongguang Fine Chemicals Company (Beijing, China) and were utilized without additional purification.

Synthesis of BOH and BOE, were briefly described as follows (Scheme 1). 4-(Octyloxy) benzaldehyde (or 4-carboxybenzaldehyde) and 2,4-dimethylpyrrole with the molar ratio of 1 : 2 were dissolved in dry tetrahydrofuran (or dichloromethane) under nitrogen atmosphere. Catalytic amount of trifluoroacetic acid (TFA) and 1 molar equivalent of 2,3-dichloro-5,6-dicyano-1,4-benzoquinone (DDQ) were added in the reaction solution. After stirred for 3 hours, Et_3N and BF_3OEt_2 were successively added into the reaction mixture, and then were treated by water, brine, and anhydrous Na_2SO_4 successively. The crude product was purified by silica gel column chromatography to obtain BOE′ (or BOH′). BOE′ (or BOH′) and 3 molar equivalents of *p*-hydroxybenzaldehyde were mixed with toluene, piperidine and acetic acid, and the working solution were refluxed for 17 hours. After cooling to room temperature, the reaction mixture was treated, dried and concentrated. The crude compound was purified by silica gel column chromatography to give BOE (or BOH). More detailed information was shown in ESI.†

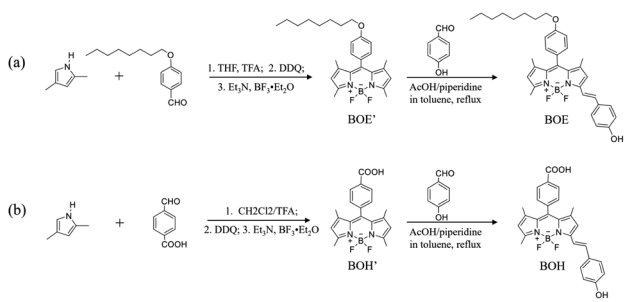

Scheme 1 The synthetic routes of target compounds.

The ^1H NMR was recorded by Bruker AM-400 MHz NMR spectrometer (Bruker, Karlsruhe, Germany) and ^{13}C NMR spectra was recorded by Bruker AM-600 MHz NMR spectrometer (Bruker, Karlsruhe, Germany). High Resolution Mass Spectrometry (HRMS) data were obtained by Thermo Fisher Q Exactive (Waltham, MA, USA) using positive mode electron spray ionization (ESI). The UV-vis spectra were measured using a Cary 60 UV-vis spectrophotometer (Agilent, California, USA). Fluorescence spectra were collected with a FS5 Spectrofluorometer (Edinburgh Instruments, Edinburgh, UK). Bright field microscopic images were recorded by TE-2000U inverted fluorescence microscope (Nikon Corporation, Tokyo, Japan).

The confocal fluorescent images were recorded by the Leica TCS SP8 confocal machine (Leica, Wetzlar, Germany). HPLC-MS spectra were obtained using Acquity UPLC-Xevo G2 QTof (Waters, Milford, MA). And the chromatography experiment was conducted using a Waters UPLC HSS T3 column with dimensions of 2.1 mm internal diameter and 100 mm length, and a particle size of 1.8 μm. The mobile phases were composed of phase A (acetonitrile : water = 6 : 4, containing 0.1% formic acid and 5 mM ammonium formate) and phase B (isopropanol : acetonitrile = 9 : 1, also containing 0.1% formic acid and 5 mM ammonium formate). The data analysis for this chromatography experiment was performed using the Thermo Scientific Xcalibur software.

2.2 Experimental methods

2.2.1 Preparation of giant unilamellar vesicles (GUVs) samples. GUVs were prepared using an electroformation method with modifications.[44] The cell used for GUV preparation consisted of two indium tin oxide (ITO) glass substrates separated by a Teflon spacer with a thickness of ~3 mm. PC reagent dissolved in chloroform at a concentration of 4 mg mL^{-1} containing BOH (or BOE) (10^{-5} M) pre-dissolved in ethanol was mixed at a 1 : 1 ratio by volume, and 100 μL of the mixed solution was dropped onto each ITO plate. After drying in vacuum for 1.5 h to remove residual solvent, two such ITO plates were glued to a polytetrafluoroethylene frame to form a closed cell. Subsequently, 1.0 mL of sucrose solution (0.1 M) was injected into the cell, which was sealed using silicone grease. Alternating electrical fields from a Rigol DG1022U function generator (Rigol Technologies, Beijing, China) were applied to the cell to generate a turbid GUV suspension with a volume of approximately 1.0 mL. The experiments were conducted at ambient temperature (25 ± 2 °C).

2.2.2 Morphological characterization of GUVs. Real-time morphological changes of GUVs were monitored by bright field image mode using an inverted fluorescence microscope, with images examined by a Cascade II 512 semiconductor-cooled CCD (Photometrics Inc., Tucson, USA) with a resolution of 512 × 512 pixels. A 200 μL liposome suspension was added to a Costar 24-well cell culture cluster (Corning Incorporated, Corning, USA) and placed on the microscope table. After adding NaClO, morphological images of GUVs were collected every 1 s over 30 min. GUVs without antioxidant were used as blank samples, and those with BOH (or BOE) were used as experimental groups, respectively.

2.2.3 Fluorescence imaging of GUVs samples. Confocal microscopy was used to observe fluorescence changes of GUVs containing BOH (or BOE) at different time points (1, 5, 10, 15, 25 minutes) after the addition of NaClO (5×10^{-5} M), photographs were taken every minute for a total of 30 times. Excitation light sources were 488 nm and 552 nm, corresponding to detection ranges of 500–550 nm and 570–600 nm, respectively. A 60× oil immersion objective lens was used for observation. The captured images were analyzed using Leica simulator SP8 software with a resolution of 1024 × 1024. GUVs were fixed using agarose. All experiments were repeated for observation on at least three GUVs by confocal imaging.

2.2.4 Fluorescence kinetics of BOH (or BOE) reacting with NaClO by stop-flow method. Kinetic studies of the reactions of BOH and BOE with NaClO, respectively, were carried out using the RX2000 Rapid-Mixing Stop-Flow Unit (Applied Photophysics Ltd, Surrey, UK) combined with an FS5 Spectrofluorometer. One syringe contained NaClO aqueous solution with a final concentration of 5×10^{-5} M, while the other syringe contained BOH or BOE ethanol solution or GUVs solution with a final concentration of 5×10^{-7} M. The peaks of raw materials and products were detected respectively. In the ethanol–water (1 : 1) homogeneous system, detection wavelengths for BOH were 592 nm and 520 nm, and those for BOE were 586 nm and 530 nm. In the GUVs heterogeneous system, detection wavelengths for BOH were 592 nm and 530 nm, and those for BOE were 595 nm and 530 nm.

2.2.5 Theoretical studies. Conformations of fluorophores in ethanol at the ground state were optimized *via* DFT calculations at the B3LYP/6-311G+(d, p) level of theory using the Gaussian 16 computational package.[45] The self-consistent reaction field (SCRF) method combined with the integral equation formalism (IEF) polarized continuum model (PCM) solvation model was employed, with an ethanol solvent model. These optimizations ensured the absence of imaginary frequencies, confirming that the optimized structures represented energy minima. To analyze the behavior of BOH and BOE in lipid membranes, classical molecular dynamics (MD) simulations were performed. The structural libraries of lipid molecules and bilayers used in Membrane Builder are available at the CHARMM-GUI website. A single molecule of either BOH or BOE was embedded in a 1,2-dioleoyl-*sn*-glycero-3-phosphocholine (DOPC) bilayer consisting of 128 lipid molecules (64 in each leaflet) and 5960 water molecules (2980 for each side). DOPC bilayers are commonly used as minimalistic models of cell membranes. Simulated DOPC bilayers had a membrane thickness of 37.0 ± 0.2 Å. The formal concentration of fluorophores in the membrane was thus <1 mol%.[46] Several pulling trajectories with varying orientations of the inserted molecules were performed, and stable insertion geometries were considered for further production runs. While the BOH molecule was not stably localized inside the bilayer and desorbed to the lipid–water interface, the BOE molecule was stably localized inside the bilayer. Each MD trajectory of membranes with an embedded fluorophore was simulated for 100 ns. Stabilization of fluorophore localization depth and orientation in the bilayer were used as the main equilibration criteria. Typical parameters for MD simulations of lipid bilayers were employed, including periodic boundary conditions, semi-isotropic Parrinello-Rahman barostat with 1 bar pressure, and Nose–Hoover thermostat with a temperature of 303 K.[47,48] All classical MD simulations were performed using the GROMACS (version 2020.6) software suite.

3 Results and discussions

Scheme 2 illustrates the molecular structures (a) and the optimized conformations (b) of BOH and BOE. The dihedral angles between the dipyrrole plane and styryl group are depicted in (a), with the phenol styryl group highlighted in a dashed square. The conformational optimization, based on DFT calculations, reveals that both BOH and BOE in ethanol solution adopt similar conformations characterized by the C8-phenyl group being perpendicular to the styryldipyrrolic π-systems (Scheme 2b). This implies that the C8-substituent group primarily contributes to the BODIPY π-systems through electronic effects rather than conjugation effects.

3.1 Physicochemical properties and the reaction mechanism of two styryl BODIPYs with ClO^-

Fig. 1 displays the absorption and fluorescence emission spectra of BOH (red) and BOE (black) measured in ethanol solution. These two molecules exhibit almost identical conjugation structures and conformations, resulting in similar spectral patterns, as indicated in Scheme 2. Compared to their synthetic precursors (BOE′ and BOH′), they demonstrate significantly red-shifted (~70 nm) absorption maxima due to the introduction of conjugated styryl groups. Both molecules emit orange fluorescence. The *ortho*-C substituents of the C8-phenyl group, octyloxy for BOE and carboxyl for BOH, possess different electron-donating capabilities, resulting in slight shifts in spectral maxima (λ_{max}(abs) or λ_{max}(em)) between the two molecules (as observed in Fig. 1 and summarized in Table 1). The fluorescence quantum yields of both styryl

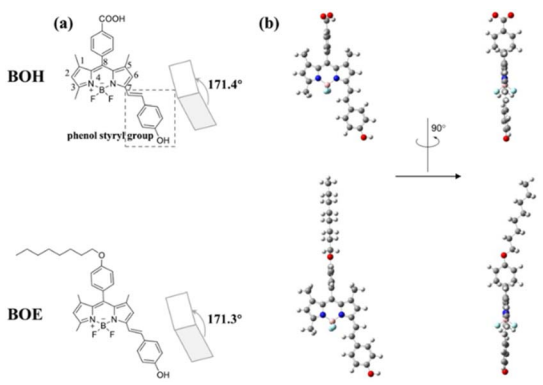

Scheme 2 The molecular structures (a) and the optimized conformations (b) of BOH and BOE. The dihedral angles between dipyrrole plane and styryl group were present in (a). The conformational optimization was performed based on DFT calculations. The phenol styryl group were shown in dashed square.

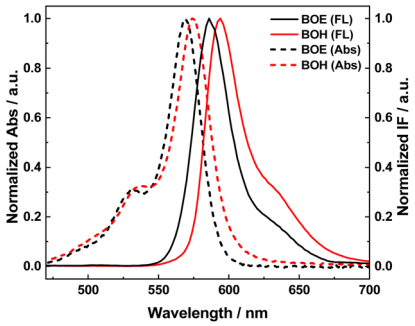

Fig. 1 Normalized absorption (dashed lines) and fluorescence emission (solid lines) spectra of BOH (red) and BOE (black) measured in ethanol solution. For fluorescence spectra measurement, all samples were excited at 400 nm.

BODIPYs exceed 80%, indicating their potential as fluorescent probes. Lipophilicity, evaluated by the oil–water distribution coefficient (Log P) (see Table 1), reveals that BOE is more lipophilic than BOH due to the hydrophobic *n*-octyloxy group introduced instead of the hydrophilic carboxyl group at the *ortho*-position of the C8-phenyl.

Fig. 2 compares the fluorescence spectra of BOH (and BOE) before (red) and after (black) reacting with ClO^- in ethanol/PBS buffer (1 : 1, v/v, pH = 7.2–7.4) mixing solution and in GUV suspensions, respectively. The spectra of synthetic precursors for the two fluorescent probes are also presented as references (gray). The concentration of ClO^- is 100 times that of the fluorophores. In both reaction media, oxidation of the fluorescent probes by ClO^- generates two spectral species. The longer-wavelength emitting species corresponds to the unreacted styryl BODIPY, while the shorter-wavelength emitting species corresponds to the oxidized product. TLC analysis confirmed this assignment. The oxidized products exhibit similar spectral characteristics to their synthetic precursors, emitting green fluorescence. These results suggest that these fluorophores may be developed into fluorescent probes with color-change mechanisms upon reaction with ClO^- in either homogeneous solution or heterogeneous liposome suspensions. Additionally, in ethanol solutions, the unreacted fluorophores exhibit slightly blue-shifted spectra compared to those before the reaction, attributed to the environmental change from pure ethanol (before reaction) to the ethanol/PBS buffer mixture (after reaction). In GUVs (pH = 7.0), the unreacted fluorophores show slightly red-shifted spectra compared to those before the reaction, attributed to the polarity change of lipid bilayers upon oxidation by ClO^- (the mechanism will be discussed later).

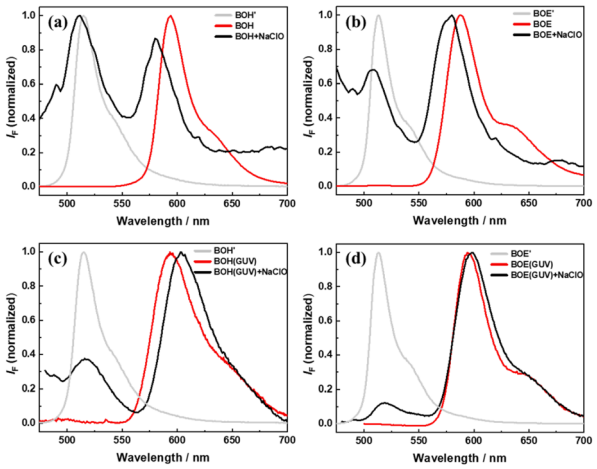

Fig. 2 Normalized fluorescence emission spectra of BOH (a and c) and BOE (b and d) reaction without and with ClO^-/HClO in ethanol solution (a and b) and in GUVs (c and d), respectively. The concentration of fluorophores was adjusted as 5×10^{-7} M, and ClO^-/HClO was 5×10^{-5} M prepared in PBS buffer (pH = 7.2–7.4). The spectra of BOE′ and BOH′ (in gray), the synthetic precursors of BOE and BOH, respectively, were present as reference. The excitation wavelength for all the measurements were at 400 nm. All spectra were measured after reaction for 1 min.

High-resolution mass spectrometry (HRMS) was employed to explore the reaction mechanism of BOH and BOE oxidized by ClO^- in ethanol solutions. The deduced intermediate structures are listed and displayed in Scheme 3, indicating that the reaction with ClO^- primarily occurs at the central vinyl group (on the styryl group) to yield chlorohydrin (or epoxide) for BOH (or BOE). Subsequent cleavage of the C–C bond produces the dipyrrolic aldehyde and phenols. Similar mechanisms were proposed for other styryl-BODIPY derivatives.[49]

3.2 Fluorescent kinetics of two styryl BODIPYs reaction with ClO^-

Fig. 3 illustrates the early-stage kinetics (within several tens of seconds) of the oxidation reaction of two fluorophores by ClO^- in ethanol/buffer mixing solution and in GUVs, measured by fluorescent spectra combined with stop-flow method. Representative fluorescence wavelengths were selected to monitor the evolution of unreacted fluorophores and the oxidized product.

Table 1 Physicochemical properties of BOE and BOH

Compound	$\lambda_{max}^{abs\ a}$/nm	$\lambda_{max}^{em\ a}$/nm	Log P^b	Φ^a/%
BOE	569	586	2.25	81.85
BOH	574	594	1.00	87.73

[a] The photophysical property data were acquired in an ethanol solution, and Φ is the fluorescence quantum yield. [b] The photophysical property data were acquired in an octanol solution of the corresponding compound. Log *P* is the oil/water distribution coefficient.

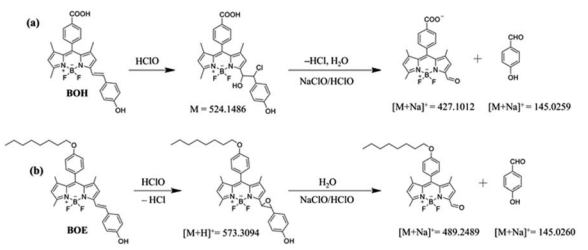

Scheme 3 Proposed reaction mechanisms of ClO^-/HClO with BOH (a) and BOE (b).

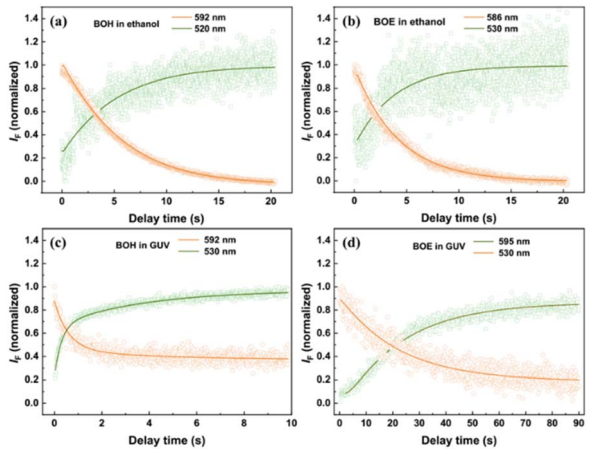

Fig. 3 Reaction kinetics probing at representative emission wavelengths by fluorescence spectrophotometer combining stop-flow technique. The working solution with NaClO (5×10^{-5} M) and fluorophores (5×10^{-7} M) in ethanol solution (a and b) and in lipid bilayers sucrose solutions (c and d), respectively. The probing wavelengths were 592 and 520 nm (a), 586 and 520 nm (b), 592 and 530 nm (c), and 595 and 530 nm (d), respectively.

Overall, similar kinetic correlation patterns were observed across all samples. The decrease in orange fluorescence species was synchronous with the increase in green fluorescence species, indicating kinetic correlation between the two fluorescent species. Additionally, the kinetic curves for each sample could be perfectly fit by the same mono- or bi-exponential functions. The reaction rates (in s^{-1}) and their corresponding amplitudes (in %) are listed in Table 2. For BOH, bi-exponential kinetics were observed, with the major component (~89% in amplitude) exhibiting a much larger reaction rate (eight times that obtained in homogeneous solution) than the minor one (~11% in amplitude, with a rate approximately two-thirds of that measured in homogeneous solution). For BOE, mono-exponential kinetics were observed, with the reaction rate determined to be approximately one-sixth of that measured in homogeneous solution. This difference will be further explained and discussed in the next section, considering the various locations of the two styryl BODIPYs in lipid bilayers.

It's worth noting that the fluorescence intensity of unreacted fluorophores measured in GUVs only decayed to 40% (or 20%) of their original levels within the measuring time range. Further kinetic evolution of the fluorophores will be studied using different methods and discussed over longer time frames.

Table 2 Fluorescent kinetics fitting results of BOH (BOE) (5×10^{-7} M) reacting with ClO^-/HClO (5×10^{-5} M) measured in ethanol solution or in GUVs suspension, respectively

Sample	Rate (s^{-1}) (amplitude, %)
BOH in ethanol	0.24 (100)
BOE in ethanol	0.26 (100)
BOH in GUVs	2.00 (88.7)
	0.16 (11.3)
BOE in GUVs	0.042 (100)

To investigate the probing effect of the two styryl BODIPY derivatives in GUVs on aqueous ClO^-, real-time fluorescence microscopic images were captured using a fluorescence confocal microscope, as shown in Fig. 4a and b. The same concentrations of fluorophores and ClO^- were used as in the stop-flow measurement. The fluorescence kinetics over a much longer time range (30 minutes) were recorded based on the fluorescence intensity. Images captured at the red and green channels corresponded to unreacted fluorophores and the oxidative product, respectively.

For BOH (Fig. 4c), the fluorescence intensity measured in the red channel gradually decreased to zero over 30 minutes. The fluorescence intensity measured in the green channel exhibited a two-phase kinetics pattern. Initially, for the first 17 minutes, the oxidative product increased accompanied by the decay of raw materials (red channel species). Subsequently, in the remaining time, the green channel species also decayed, implying that the oxidized product of BOH was further oxidized to non-fluorescent species due to the excess amount of ClO^- added.

For BOE (Fig. 4d), the fluorescence intensity measured in the red channel linearly decayed by approximately 70% over 30 minutes. Concurrently, a linear and slower decay of the green channel species occurred, attributed to the combined kinetics of the green channel species, including both the generation and reoxidation of the oxidized product. Since fluorescent confocal imaging measurements required at least two minutes for preparation and focusing, the very early-stage kinetics couldn't be accurately observed.

In summary, for both BOH and BOE in GUVs, the fluorescence change of the raw material was more sensitive than that of the oxidized product in reflecting reactions with aqueous ClO^-. BOE appears to be more stable than BOH in GUVs against oxidation by aqueous ClO^-.

3.3 Protective effect of two styryl BODIPYs on lipid bilayers against oxidation by ClO^-

To monitor the protective effect of these two fluorophores on liposomes, the morphological changes of GUVs over time upon oxidation by ClO^-, with and without the presence of BOH or BOE, were measured using bright-field mode on an inverted fluorescence microscope. The concentration of NaClO was increased by 20 times compared to previous measurements to induce obvious morphological changes in liposomes within 30 minutes. Oxidation by ClO^- caused the collapse of GUV structure in less than 4 minutes, as observed in Fig. 5b. In comparison, the presence of embedded BOH or BOE significantly delayed the onset of observable morphological changes in GUVs. With 5×10^{-7} M BOH, the same concentration of ClO^- (1×10^{-3} M) started to induce surface roughening and budding of GUVs after more than 10 minutes (Fig. 5c). In contrast, with the same amount of embedded BOE, the GUV remained intact until 30 minutes later (Fig. 5d). These results demonstrate that BOE exhibits a more excellent protective effect than BOH on GUVs against oxidation by ClO^-.

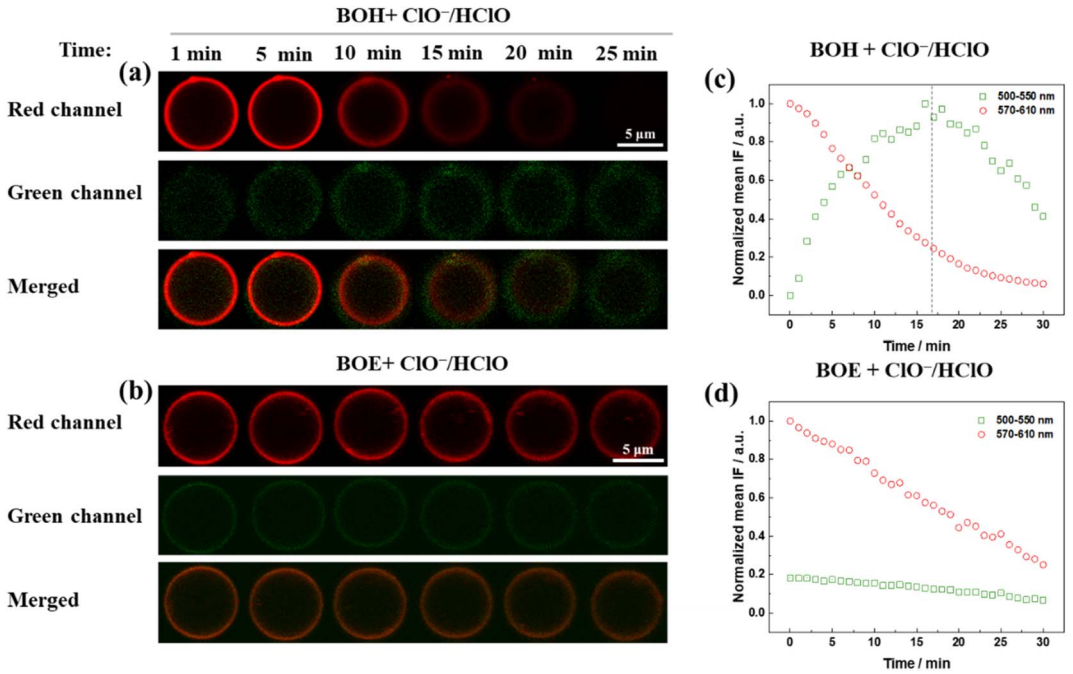

Fig. 4 Real-time fluorescent microscopic images of GUVs containing 5×10^{-7} M fluorophores with addition of 5×10^{-5} M NaClO. Fluorescence signal of GUVs were collected in the range of 570–610 nm (red channel) and 500–550 nm (green channel) under excitation at 552 and 488 nm, respectively. The merged images were present too. The fluorescent intensity kinetics of images were shown as (c) and (d). All the measurements were performed 2 minutes later the working solution prepared.

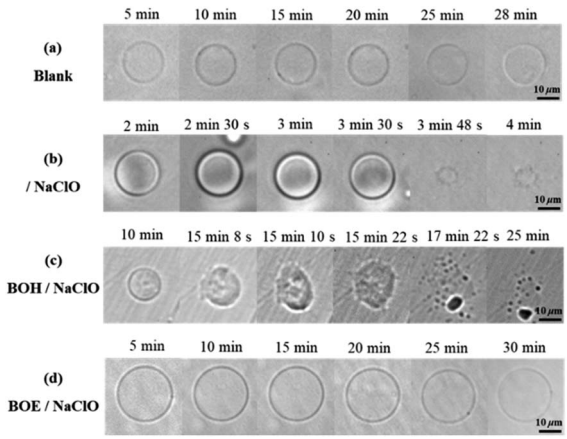

Fig. 5 Bight field microscopic images of GUV morphological change induced by ClO^-/HClO oxidation over time. (a) Blank GUV (control); (b) blank GUV oxidized by NaClO (1×10^{-3} M); (c) GUV containing BOH (5×10^{-7} M) oxidized by NaClO (1×10^{-3} M); (d) GUV containing BOE (5×10^{-7} M) and NaClO (1×10^{-3} M). Scale bar = 10 μm.

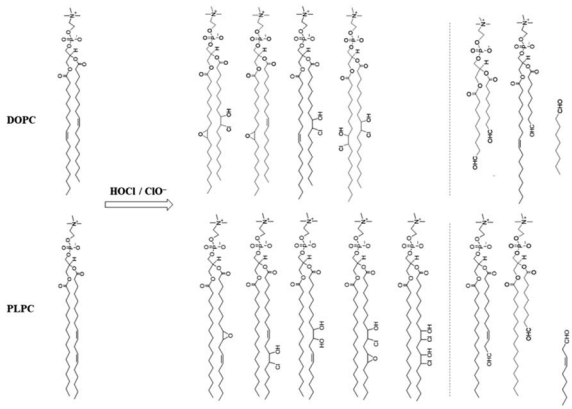

Scheme 4 Proposed reaction mechanisms of ClO^-/HClO with two main phosphatidylcholines species in GUV, *i.e.* DOPC and PLPC, respectively, based on the HPLC-MS results shown as Fig. S8 in ESI.†

3.4 Protective mechanisms of two styryl BODIPYs on lipid bilayers against oxidation by ClO^-

To further understand why BOE exhibits a much better protective effect than BOH, investigations into the oxidation mechanism of lipids by ClO^- were conducted using the HPLC-MS method. The results, depicted in Fig. S8 in the ESI,† led to the proposed mechanism outlined in Scheme 4. The lipids used in this study contain 14–29% L-α-phosphatidylcholine, with PLPC (with linoleic acid, 60%) and DOPC (with oleic acid, 10%) being the main components. Based on the HR-MS results of the main products observed in the HPLC profile, the oxidation mechanism was proposed. Clearly, the oxidation of DOPC and PLPC by ClO^- predominantly occurred at the vinyl groups located at the center of hydrophobic fatty acid tails, resulting in mono-and bi-adducts of chlorohydrins, epoxides, and aldehyde derivatives (chain broken products). The generation of much polar oxidative products causes a turnover of hydrophobic fatty acid tails, leading to GUV roughening, budding, and eventual collapse. Similar mechanisms have been reported for GUVs oxidized by other ROS.[50,51]

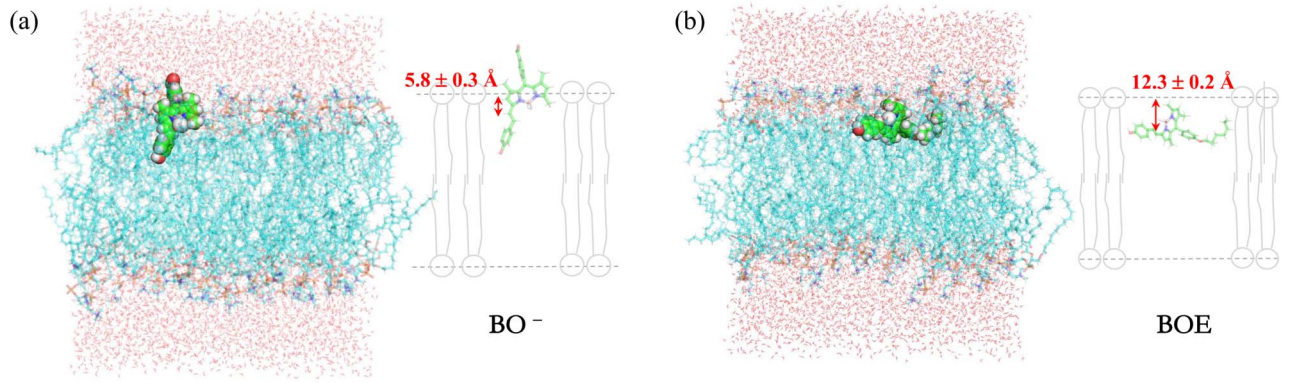

Fig. 6 Snapshots depicting configuration and the average position (statistically calculated in 100 ns equilibration time) of BOH (in BO^- form) (a) and BOE (b) simulated in lipid membrane. Color coding: for DOPC, lipid headgroups, orange; lipid tails, cyan; for fluorophores, carbon atoms, green balls; hydrogen atoms, white balls; oxygen atoms, red balls; nitrogen atoms, blue balls; fluoride, grey balls; boron atoms in fluorophores, pink balls; water is depicted in red sticks. The right scheme of each figure stresses the location of central vinyl group referred to the head group surface of lipids (pointed out by red arrows).

Further quantitative analysis of the oxidative products of lipids under the protection of BOH (or BOE), shown in Fig. S9 in the ESI,† indicated that with embedded BOH (or BOE), the amount of lipid oxidized product decreased significantly. Specifically, for BOH, the reductions were 60% (DOPC-ClOH), 61% (DOPC-$Cl_2(OH)_2$), and 51% (PLPC-$Cl_2(OH)_2$), whereas for BOE, they were 72% (DOPC-ClOH), 84% (DOPC-$Cl_2(OH)_2$), and 80% (PLPC-$Cl_2(OH)_2$), respectively. Clearly, the protective effect of BOE is superior to that of BOH.

Based on all the aforementioned results, we endeavoured to discuss why BOE has a better protective effect than BOH on GUVs against oxidation by ClO^-. To address this question, molecular dynamics simulations were performed, and the results are shown in Fig. 6. A 100 ns dynamics simulation of one fluorophore embedded in a lipid-bilayer model was conducted. After equilibration, the results indicated that: (1) BOH (in BO^- form) stays at the interface of lipid-water phases, with the vinyl group, the most reactive group of styryl BODIPYs as determined above, approximately 5.8 ± 0.3 Å below the polar surface of phosphatidylcholine (PC). (2) BOE, due to its more hydrophobic property, resides deeper in the lipid phase than BOH. The vinyl group is approximately 12.3 ± 0.2 Å below the polar surface of PC, which is comparable to the unsaturated vinyl groups of fatty acids on lipids. Since the unsaturated double bonds on fatty acids were their main oxidative targets of ClO^- as proved above, BOE would provide more protective effect on GUVs than BOH, as evidenced by the morphological imaging results of GUVs.

4 Conclusions

In this research, two styryl BODIPY derivatives with different hydrophilicity were synthesized and studied for their reaction mechanisms with ClO^- in homogeneous ethanol solutions and in heterogeneous GUVs, respectively, using experimental and theoretical methods. DFT calculations confirmed that the optimized conformations of these two derivatives were the same. Fluorescence spectra and high-resolution mass spectra revealed that the central vinyl group was the common anti-oxidation group for them against oxidation by ClO^-. In homogeneous ethanol/water mixing solutions, the two derivatives exhibited similar mechanisms and kinetics of reaction with ClO^-. Conversely, in GUVs, these two styryl BODIPYs demonstrated different kinetics. BOE was found to provide more efficient protection than BOH to GUVs. Assisted by molecular dynamics simulation, the underlying mechanism was proposed. Due to the introduction of the more lipophilic octyloxy group, BOE remains deeper in the lipid phase than BOH, where its vinyl group is located more proximately to the corresponding target group of lipids, *i.e.*, the unsaturated double bond on fatty acids, thus providing better protection. This work not only establishes the two styryl BODIPYs as promising candidates for fluorescent probes for the detection of ClO^- in various environments but also offers guidance for molecular design in this field.

Data availability

The authors confirm that the data supporting the findings of this study are available within the article and its ESI.†

Author contributions

Conceptualization, L. Y. and Y. L. J; methodology, L. Y. and Y. L. J; validation, L. Y. and Y. L. J; investigation, L. Y., Q. W. L. and A. L. S; resources, M. Q. C. and A. L. S.; data curation, L. Y. and Y. L. J; writing—original drapreparation, L. Y.; writing—review and editing, P. W.; supervision, J. P. Z. All authors have read and agreed to the published version of the manuscript.

Conflicts of interest

The authors declare no competing financial interest.

Acknowledgements

This work has been supported by the Natural Science Foundation of China (21673289). The computer resources were provided by Public Computing Cloud Platform of Renmin University of China.

Notes and references

1 E. Hidalgo, R. Bartolome and C. Dominguez, *Chem.-Biol. Interact.*, 2002, **139**, 265–282.
2 C. C. Winterbourn, M. B. Hampton, J. H. Livesey and A. J. Kettle, *J. Biol. Chem.*, 2006, **281**, 39860–39869.
3 M. B. Hampton, A. J. Kettle and C. C. Winterbourn, *Blood*, 1998, **92**, 3007–3017.
4 Y. W. Yap, M. Whiteman and N. S. Cheung, *Cell Signalling*, 2007, **19**, 219–228.
5 C. C. Winterbourn, *Toxicology*, 2002, **181–182**, 223–227.
6 O. M. Panasenko, I. V. Gorudko and A. V. Sokolov, *Biochemistry*, 2013, **78**, 1466–1489.
7 S. Baldus, C. Heeschen, T. Meinertz, A. M. Zeiher, J. P. Eiserich, T. Münzel, M. L. Simoons and C. W. Hamm, *Circulation*, 2003, **108**, 1440–1445.
8 J. K. Andersen, *Nat. Med.*, 2004, **10**, S18–S25.
9 S. J. Nicholls and S. L. Hazen, *Arterioscler., Thromb., Vasc. Biol.*, 2005, **25**, 1102–1111.
10 Y. Yue, F. Huo, C. Yin, J. O. Escobedo and R. M. Strongin, *Analyst*, 2016, **141**, 1859–1873.
11 R. Zhang, B. Song and J. Yuan, *Trends Anal. Chem.*, 2018, **99**, 1–33.
12 S. Debnath, R. Ghosh, R. R. Nair, D. Pradhan and P. B. Chatterjee, *ACS Omega*, 2022, **7**, 38122–38149.
13 V. T. Cheshchevik, N. G. Krylova, N. G. Cheshchevik, E. A. Lapshina, G. N. Semenkova and I. B. Zavodnik, *Biochimie*, 2021, **184**, 104–115.
14 H. Shangguan, Q. Liu, Y. Wang, Z. Teng, R. Tian, T. Wu, L. Yang, L. Jiang, X. Liu and L. Wei, *Spectrochim. Acta, Part A*, 2023, **303**, 123256.
15 L. Wang, G. Fang and D. Cao, *Sens. Actuators, B*, 2015, **207**, 849–857.
16 X. Qu, Y. Bian, Y. Bai and Z. Shen, *Chin. J. Inorg. Chem.*, 2019, **35**, 649–657.
17 S. Jantra, T. Palaga, P. Rashatasakhon, M. Sukwattanasinitt and S. Wacharasindhu, *Dyes Pigm.*, 2021, **191**, 109341.
18 Z. Xue, T. Liu and H. Liu, *Dyes Pigm.*, 2019, **165**, 65–70.
19 Y. Ji, L.-J. Xia, L. Chen, X.-F. Guo, H. Wang and H.-J. Zhang, *Talanta*, 2018, **181**, 104–111.
20 J. Shao, H. Guo, S. Ji and J. Zhao, *Biosens. Bioelectron.*, 2011, **26**, 3012–3017.
21 S. Wang, H. Liu, J. Mack, J. Tian, B. Zou, H. Lu, Z. Li, J. Jiang and Z. Shen, *Chem. Commun.*, 2015, **51**, 13389–13392.
22 H.-W. Liu, X. Zhu, J. Zhang, X.-B. Zhang and W. Tan, *Analyst*, 2016, **141**, 5893–5899.
23 C. Chan, W. Zhang, Z. Xue, Y. Fang, F. Qiu, J. Pan and J. Tian, *Anal. Chem.*, 2022, **94**, 5918–5926.
24 M. S. Purdey, H. J. McLennan, M. L. Sutton-McDowall, D. W. Drumm, X. Zhang, P. K. Capon, S. Heng, J. G. Thompson and A. D. Abell, *Sens. Actuators, B*, 2018, **262**, 750–757.
25 J. Xu, Q. Li, Y. Yue, Y. Guo and S. J. Shao, *Biosens. Bioelectron.*, 2014, **56**, 58–63.
26 C. Gao, L. Lin, W. Sun, Z. L. Tan, J. R. Huang, L. He and Z. L. Lu, *Talanta*, 2018, **176**, 382–388.
27 X. Lv, Y. Wang, S. Zhang, Y. Liu, J. Zhang and W. Guo, *Chem. Commun.*, 2014, **50**, 7499–7502.
28 X. Zhao, C. Gao, N. Li, F. Liu, S. Huo, J. Li, X. Guan and N. Yan, *Tetrahedron Lett.*, 2019, **60**, 1452–1456.
29 X. Qu, W. Song and Z. Shen, *Front. Chem.*, 2019, **7**, 598.
30 X. Wang, Y. Tao, J. Zhang, M. Chen, N. Wang, X. Ji and W. Zhao, *Chem.–Asian J.*, 2020, **15**, 770–774.
31 S. Jantra, P. Butta, P. Jithavech, P. Rojsitthisak, T. Palaga, P. Rashatasakhon, M. Sukwattanasinitt and S. Wacharasindhu, *Dyes Pigm.*, 2019, **162**, 189–195.
32 C. Huang and Y. Qian, *Opt. Mater.*, 2019, **92**, 53–59.
33 G. Li, D. Ji, S. Zhang, J. Li, C. Li and R. Qiao, *Sens. Actuators, B*, 2017, **252**, 127–133.
34 H. Li, Y. Miao, Z. Liu, X. Wu, C. Piao and X. Zhou, *Dyes Pigm.*, 2020, **176**, 108192.
35 X. Xu and Y. Qian, *Spectrochim. Acta, Part A*, 2017, **183**, 356–361.
36 D. Ji, G. Li, S. Zhang, M. Zhu, C. Li and R. Qiao, *Sens. Actuators, B*, 2018, **259**, 816–824.
37 H. Zhu, Z. Zhang, S. Long, J. Du, J. Fan and X. Peng, *Nat. Protoc.*, 2018, **13**, 2348–2361.
38 L. A. Bagatolli and D. Needham, *Chem. Phys. Lipids*, 2014, **181**, 99–120.
39 R. Itri, H. C. Junqueira, O. Mertins and M. S. Baptista, *Biophys. Rev.*, 2014, **6**, 47–61.
40 E. E. Ambroggio, F. Separovic, J. H. Bowie, G. D. Fidelio and L. A. Bagatolli, *Biophys. J.*, 2005, **89**, 1874–1881.
41 S. L. Veatch and S. L. Keller, *Biophys. J.*, 2003, **85**, 3074–3083.
42 H. G. Döbereiner, J. Käs, D. Noppl, I. Sprenger and E. Sackmann, *Biophys. J.*, 1993, **65**, 1396–1403.
43 K. A. Riske and H. G. Döbereiner, *Biophys. J.*, 2003, **85**, 2351–2362.
44 M. I. Angelova, S. Soléau, Ph. Méléard, F. Faucon and P. Bothorel, *Prog. Colloid Polym. Sci.*, 1992, **89**, 127–131.
45 M. J. Frisch, G. W. Trucks, H. B. Schlegel, G. E. Scuseria, M. A. Robb, J. R. Cheeseman, G. Scalmani, V. Barone, G. A. Petersson and H. Nakatsuji, *Gaussian 16, Revision A.03*, Gaussian, Inc., Wallingford CT, USA, 2016.
46 M. Pederzoli, M. Wasif Baig, M. Kývala, J. Pittner and L. Cwiklik, *J. Chem. Theory Comput.*, 2019, **15**, 5046–5057.
47 M. Parrinello and A. Rahman, *J. Appl. Phys.*, 1981, **52**, 7182–7190.
48 S. Nosé, *Mol. Phys.*, 1984, **52**, 255–268.
49 S. Jantra, P. Butta, P. Jithavech, P. Rojsitthisak, T. Palaga, P. Rashatasakhon, M. Sukwattanasinitt and S. Wacharasindhu, *Dyes Pigm.*, 2019, **162**, 189–195.
50 K. K. Fan, Y. M. Zhou, Y. Wei, R. M. Han, P. Wang, L. H. Skibsted and J. P. Zhang, *Biophys. Chem.*, 2022, **285**, 106807.
51 Y. Wei, Y. M. Zhou, Y. Q. Li, R. Y. Gao, L. M. Fu, P. Wang, J. P. Zhang and L. H. Skibsted, *Biophys. Chem.*, 2021, **275**, 106624.